



RESEARCH ARTICLE | SEPTEMBER 27 2022

Experimental study on the formation of two axial jets of cavitation bubbles near soft membranes with different thicknesses

Ao Wang ; Yuxue Zhong; Guanghang Wang ; ... et. al

AIP Advances 12, 095023 (2022)

<https://doi.org/10.1063/5.0107339>
View
OnlineExport
Citation

CrossMark

Articles You May Be Interested In

Spreading of fast-curing, thermosetting silicones

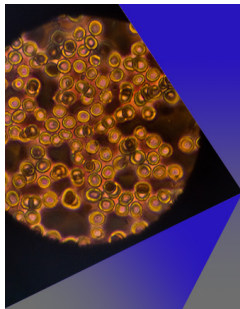
Appl. Phys. Lett. (December 2019)

A wearable mechano-acoustic sensor based on electrochemical redox reaction for continuous cardiorespiratory monitoring

Appl. Phys. Lett. (January 2021)

Elastomer based force sensor fabricated by 3D additive manufacturing

AIP Advances (January 2020)



AIP Advances

Special Topic: Medical Applications
of Nanoscience and Nanotechnology

Submit Today!

Experimental study on the formation of two axial jets of cavitation bubbles near soft membranes with different thicknesses

Cite as: AIP Advances 12, 095023 (2022); doi: 10.1063/5.0107339

Submitted: 4 July 2022 • Accepted: 1 September 2022 •

Published Online: 27 September 2022



View Online



Export Citation



CrossMark

Ao Wang,^{1,2}  Yuxue Zhong,^{1,2} Guanghang Wang,^{1,3} Jian Huang,^{1,2}  Jingzhu Wang,^{1,2,a)} 
and Yiwei Wang^{1,2,3} 

AFFILIATIONS

¹ Key Laboratory for Mechanics in Fluid Solid Coupling Systems, Institute of Mechanics, Chinese Academy of Sciences, Beijing 100190, People's Republic of China

² School of Engineering Science, University of the Chinese Academy of Sciences, Beijing 100049, People's Republic of China

³ School of Future Technology, University of the Chinese Academy of Sciences, Beijing 100049, People's Republic of China

^{a)} Author to whom correspondence should be addressed: wangjingzhu@imech.ac.cn

ABSTRACT

A cavitation bubble collapses non-spherically, splits into two smaller bubbles, and induces two axial jets flowing in opposite directions near a soft membrane. The soft membrane is deformed and even pierced after the impact of the downward jet. In this paper, we experimentally studied the formation of two axial jets of a spark-induced bubble near Ecoflex membranes with different thicknesses. Assuming that the millimeter-sized bubble is filled with an ideal gas and collapses adiabatically in water, the dominant dimensionless parameters, the stiffness (d') and stand-off distance (h^*), determining the formation of the two axial jets, are obtained, and the value of d' is varied by changing the membrane thickness. Two parameter plots for the regimes of bubble jetting and no jetting were obtained. The critical h^* of the bubble jetting increased exponentially with increasing d' , reaching a maximum of 1.1 at $d' = 0.04556$ (the thickness $d = 10$ mm). This was because the counteracting force induced by the rebounding of the deformed membrane grew in strength. After that, the h^* remained constant since the counteracting force was unchanged due to the feature changes of the membrane deformation. Consequently, we obtain a function of the boundary line between the regimes. The sub-regime of the membrane piercing was obtained in the regime of bubble jetting. It was found that the velocity of membrane deformation induced by the jet impact was an important factor in membrane piercing.

© 2022 Author(s). All article content, except where otherwise noted, is licensed under a Creative Commons Attribution (CC BY) license (<http://creativecommons.org/licenses/by/4.0/>). <https://doi.org/10.1063/5.0107339>

I. INTRODUCTION

The oscillation of a cavitation bubble near a hard rigid boundary is a classical topic in engineering fields, such as underwater acoustics, underwater explosions, and surface cleaning.^{1–6} Interest in the interaction between a cavitation bubble and a soft deformable boundary has recently been revived because of the increasing number of relevant biomedical and biological applications.^{7–10} Compared with a hard rigid boundary, a soft deformable boundary leads to a mushroom shape and elongation

and splitting of the bubble, and the bubble dynamics become more complicated.^{11–19}

Interest in the dynamics of a cavitation bubble near an elastic boundary was initially stimulated by the observations of Gibson,²⁰ who found that the liquid jet formed during bubble collapse as well as the bubble migration were both directed away from the boundary under certain conditions. Gibson and Blake^{21,22} and Blake and Gibson²³ studied the effects of the elastic properties of a rubber-coated boundary on the splitting of a spark-induced cavitation bubble. Tomita and Kodama²⁴ and Shima *et al.*²⁵ showed that when

a bubble collapsed near elastic boundaries, the boundaries affected the fluid flow around the bubbles and caused perturbation on the surface of the bubble, leading to bubble splitting and jetting. The most comprehensive experiments were done by Brujan *et al.*,^{26–28} who found that a large variation in both the jetting behavior and the deformation of the elastic boundary occurred depending on the distance between the bubble and the boundary. Subsequently, they investigated the effects of the elastic modulus of the boundary on bubble dynamics.^{27,28} For stiffer boundaries, the bubble behavior was mainly characterized by the formation of an axial liquid jet and bubble migration directed toward the boundary, as if the bubble was adjacent to a rigid wall. As mentioned above, the bubble dynamics near elastic boundaries show bubble splitting, the formation of different kinds of jets directed toward and away from boundaries, and bubble migration.

The interaction of cavitation bubbles with a thick elastic boundary has been studied extensively. However, not much has been done concerning bubble dynamics near thin elastic membranes. Shaw²⁹ was the first to report on the interactions of a cavitation bubble with a flexible membrane, employing schlieren photography and Mach–Zehnder interferometry techniques. Turangan *et al.*³⁰ conducted experimental and numerical studies of bubble–membrane interaction. They concluded that it was the curvature of the deformed membranes and not the deflection that was responsible for a pressure buildup in the fluid close to the bubble. It was also found that the shedding of toroidal bubbles, as observed near elastic boundaries, was not seen in bubbles near membranes. Orthaber *et al.*³¹ experimentally studied the effects of a cavitation bubble on a thin elastic membrane. They found that significant damage was observed at intermediate distances between the bubble and the boundary. Xu *et al.*³² investigated the effects of flexible boundaries with different elastic moduli on bubble dynamics. The results showed that as the elastic modulus of the material increased, the neck position moved toward the top of the bubble. In addition, the effects of liquid viscosity on the bubble dynamics near a membrane have been studied.^{33,34} Kan *et al.*³⁵ analyzed the interactions between spark-induced cavitation bubbles and rubble sheets with different thicknesses. The experimental results showed that sheet thickness was a dominant factor in determining the dynamics of the bubble, in addition to the parameters of the stand-off

TABLE I. Ecoflex membranes with different thicknesses.

Sample number	1	2	3	4	5	6	7	8	9	10	11	12	13
Thickness (mm)	0.3	1	2	3	4	5	6	7	8	9	10	15	20

distance and the boundary properties. However, the studies concerning the effects of membrane thickness on bubble dynamics have merely been done, and the corresponding mechanism remains unsettled.

In this paper, we experimentally investigate the bubble dynamics near an Ecoflex membrane with different thicknesses. The thickness varies from 0.3 to 20 mm. Near the soft membrane, the cavitation bubble collapses non-spherically, and thus, two axial jets form, or it collapses spherically. Consequently, we focus on the dependence of the formation of the two axial jets on the stand-off distance and membrane thickness. The work is organized as follows: Methodologies including the experimental setup and dimensional analysis are given in Sec. II, and the results and discussion are given in Sec. III. Section IV summarizes the work.

II. METHODOLOGIES

A. Experimental setup

A schematic of the experimental setup for observing the behaviors of a spark-induced cavitation bubble near an Ecoflex membrane is shown in Fig. 1. A cavitation bubble was generated using an electric discharge machine (300 V discharge voltage). A pair of copper wires with 0.3 mm diameters were used as electrodes, and their intersection point is suggested to be the initial center of the cavitation bubble.^{36,37} The Ecoflex product (No. 0030, Smooth-on, Inc.) consisted of two translucent silicon gels (i.e., part A and part B). The gels of part A and part B were mixed at a weight ratio of 1:1, stirred in a glass beaker, degassed in a vacuum drying chamber, and poured into a cylindrical mold. The mold was 90 mm in diameter with depths ranging from 0.3 to 20 mm, as presented in Table I. The soft membrane was molded after 6 h at a temperature of 25 °C. The elastic modulus of the soft membrane was determined using a tensile strength test machine with a tensile rate of 20 mm/min. The

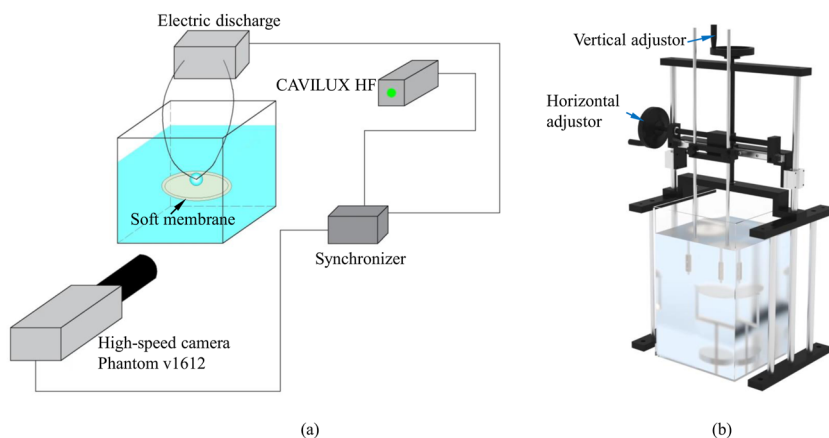


FIG. 1. A schematic of the experimental setup for observing the behaviors of a spark-induced cavitation bubble near a soft membrane: (a) experimental setup and (b) water tank with horizontal and vertical adjusters.

TABLE II. Dimensionless parameters affecting bubble jetting near soft membranes with different thicknesses.

Formula	R_m (mm)	P_∞ (Pa)	ρ_l (kg/m ³)	$\frac{P_v}{P_\infty}$	$\frac{\rho_v}{\rho_l}$	Re	We	d'	h^*
Value	12.5 ± 0.5	1.01×10^5	10^3	≈ 0	≈ 0	$\sim 10^7$	$\sim 10^4$	0.001 37–0.091 12	0.1–1.5

100% tensile modulus of the membrane used in the experiments was 62 KPa. As shown in Fig. 1(b), the membrane was fixed on a stainless-steel supporter with an inner radius of 60 mm and an outer radius of 90 mm in a water tank filled with degassed and distilled water. The tank was 300 mm in width, 300 mm in length, and 300 mm in depth.

In the experiment, the stand-off distance between the cavitation bubble and membrane was changed by turning horizontal and vertical adjusters. To eliminate the effect of spark on the observation of the initial expansion of the cavitation bubble, a pulsed laser (Cavilux HF810, 810 nm wavelength, 500 W output) with a filter was used as the light source. The laser light and a high-speed camera (V1612, Phantom Co., Ltd., USA) worked simultaneously when the electric discharge was triggered. The sampling rate of the high-speed camera was 100–130 kfps. The maximum radius of the cavitation bubble is obtained as $R_m = 12.5 \pm 0.5$ mm in an unbounded liquid in this study. Measurement uncertainty in this study was obtained by the geometric mean of two types of uncertainty components. One was induced by the gray values when the gas–liquid interface or solid–liquid interface was determined, while the other was calculated from a series of repeated observations.³⁸

B. Dimensional analysis

Near a soft membrane, a cavitation bubble collapses non-spherically, and thus, two axial jets form or it collapses spherically. This study focuses on the effects of membrane thickness on bubble jetting (i.e., the formation of two axial jets). Consequently, the main affecting parameters consist of the energy of the spark-induced cavitation bubble, the membrane thickness, the distance between the bubble and the membrane, and the properties of the liquid. The energy of the cavitation bubble is described using its initial state. As a result, the function of the bubble jetting, δ , is given,

$$\delta = f(R_0, P_0, \rho_0, \gamma, P_\infty, \rho_l, \mu_l, \sigma_s, d, E, h), \quad (1)$$

where R_0 is the initial radius of the cavitation bubble, P_0 is the initial pressure inside the bubble, ρ_0 is the initial density inside the bubble, d is the membrane thickness, E is the elastic modulus of the soft membrane, h is the distance between bubble initial center and membrane upper surface, P_∞ is the pressure in the liquid at infinity, ρ_l is the density of the liquid, μ_l is the dynamic viscosity of the liquid, σ_s is the surface tension, and γ is the ratio of the specific heats of the vapor.

Assuming that the cavitation bubble filled with ideal gas expands and contracts adiabatically, Eq. (1) is changed to Eq. (2) when $\gamma = 1.4$,

$$\delta = f(R_m, P_v, \rho_v, \gamma, P_\infty, \rho_l, \mu_l, \sigma_s, d, E, h), \quad (2)$$

where R_m is the maximum radius of the cavitation bubble in an unbounded liquid, P_v is the saturated vapor pressure, and ρ_v is the density inside the bubble at pressure P_v . Subsequently, the dimensionless parameters are obtained using the variables R_m , P_∞ , and ρ_l , as shown in the following equation:

$$\delta = f\left(\frac{P_v}{P_\infty}, \frac{\rho_v}{\rho_l}, \frac{\mu_l}{R_m \sqrt{P_\infty \rho_l}}, \frac{\sigma_s}{R_m P_\infty}, \frac{Ed}{R_m P_\infty}, \frac{h}{R_m}\right), \quad (3)$$

where $Re = \rho_l \sqrt{P_\infty \rho_l} R_m / \mu_l$ is the Reynolds number, $We = P_\infty R_m / \sigma_s$ is the Weber number, $d' = Ed / R_m P_\infty$ is the dimensionless stiffness, and $h^* = h / R_m$ is the dimensionless stand-off distance. Given the values in Table II, the effects of liquid viscosity and surface tensile are ignored. Consequently, the dominant dimensionless parameters determining the formation of the two axial jets are stiffness d' and stand-off distance h^* , as shown in the following equation:

$$\delta = f(d', h^*). \quad (4)$$

In this study, the value of d' is varied by changing the membrane thickness.

III. RESULTS AND DISCUSSION

A. Formation of two axial jets of cavitation bubble near the soft membrane

Figure 2 (multimedia view) shows the expansion and contraction of a spark-induced cavitation bubble near a soft membrane at $d' = 0.00911$ and $h^* = 0.5$. The membrane deformed as the cavitation bubble expanded. The maximum membrane deformation occurred when the bubble reached its maximum size. The cavitation bubble remained approximately spherical during the expansion, as seen in Figs. 2(b)–2(d). Subsequently, the cavitation bubble began to contract, and then, the membrane rebounded. It was found that the bubble surface close to the membrane contracted faster than the other side, thus forming a neck, as shown in Fig. 2(f). Meanwhile, an annular, disk-like flow toward the neck developed, resulting in the mushroom-like shape of the bubble described by Brujan *et al.*^{21,22} With further contraction, a low-pressure region was induced between the bubble and the membrane when the rebound velocity of the deformed membrane was smaller than the contracting velocity of the bubble, resulting in the elongation of the bubble, as seen in Fig. 2(h)–2(j). At the moment of collapse, the bubble split into two smaller bubbles from the position of the neck. A high-pressure region induced by the bubble splitting deflected the annular flow upward and downward, creating two axial jets along the symmetric axis of the vertical direction. The type of jet formation was similar to that of a high-speed jet after solid water entry,^{39–41} which was induced by bubble collapse in a thin gap⁴² and extreme vicinity to a solid boundary.^{43,44}

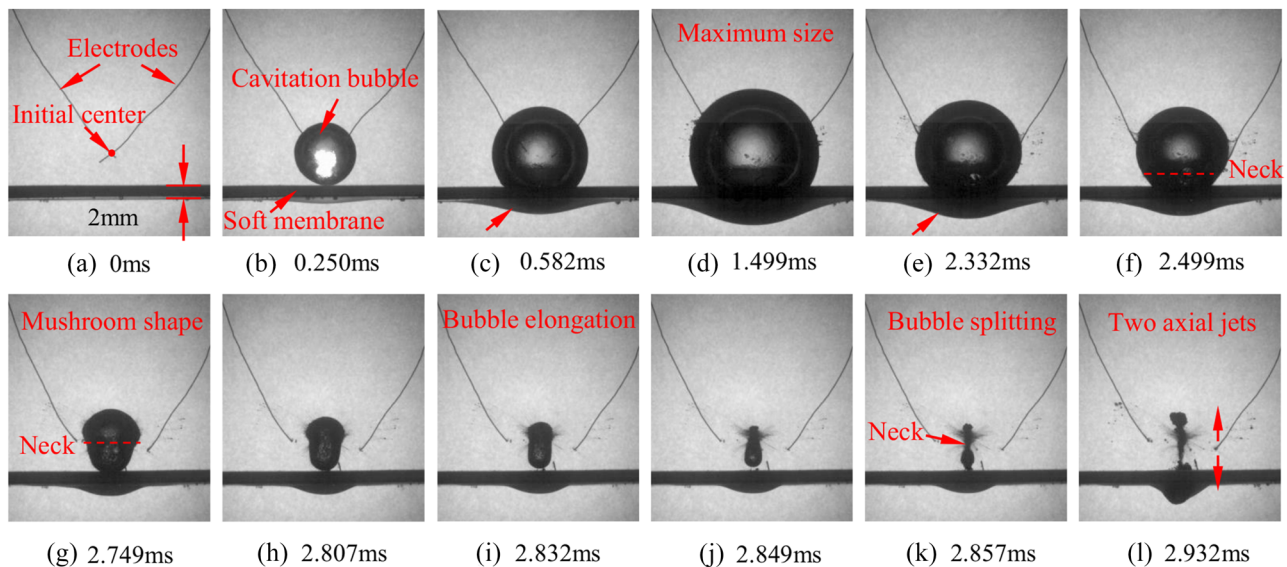


FIG. 2. Behaviors of a spark-induced cavitation bubble near a soft membrane (sample 3): bubble expansion (a)–(d) and contraction (e)–(k) at $d' = 0.00911$ and $h^* = 0.5$. In (l), the two axial jets formed move upward and downward, respectively. Multimedia view: <https://doi.org/10.1063/5.0107339.1>

When a cavitation bubble collapses near a rigid boundary, an axial jet toward the boundary is induced due to the Bjerknes force, which arises from the low-pressure region between the bubble and the boundary. In the case of a soft membrane, a counteracting force is induced by the rebounding of the deformed membrane. In addition to the Bjerknes force, as described by Brujan *et al.*,^{21,22} these two axial jets in the opposite direction are created. Consequently, the key to the formation of the two axial jets is the counteracting force, F , which is defined by the deflection, w , and the bending rigidity, D , where $F \sim wD$ according to the theory of plates and shells.⁴⁵ Here, $D = Ed^3/12(1 - \nu^2)$, where E is the elastic modulus of the membrane, d is the membrane thickness, and ν is Poisson's ratio. We know that $F \sim wd^3$ because the material of all the membranes used in this experiment was the same. The term wd^3 is used to analyze the magnitude of the counteracting force.

When the bubble splits into unequal parts from the neck position, the jet originating from the larger part of the bubble is stronger than the other jet in the opposite direction.^{25,26} To determine the energy distribution of the upward and downward migrations of the bubbles, a dimensional neck position L' is defined as $L' = L_p/L$, where L_p is the distance between the bubble point and neck position, and L is the bubble length at the moment of bubble collapse, as shown in Fig. 3.

B. Effects of dimensionless stand-off distance h^* on the formation of two axial jets

The behaviors of the cavitation bubbles after reaching their maximum sizes are investigated at $d' = 0.00911$ for various values of h^* . The experimental results showed that the characteristics of the bubble dynamics near the Ecoflex membrane could be

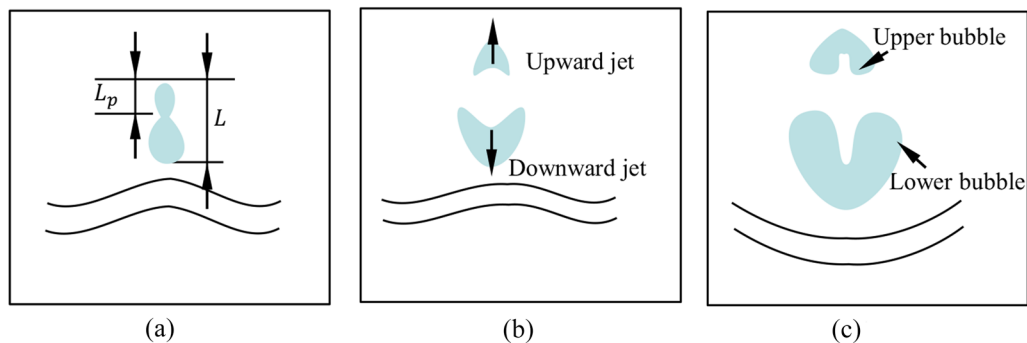


FIG. 3. Schematic of bubble splitting near a soft membrane. The dimensionless neck position $L' = L_p/L$, where L_p is the distance between the bubble's highest point and the neck position, and L is the bubble length at the moment of bubble collapse. (a) Bubble splitting, (b) Two axial jets, and (c) Bubble migration.

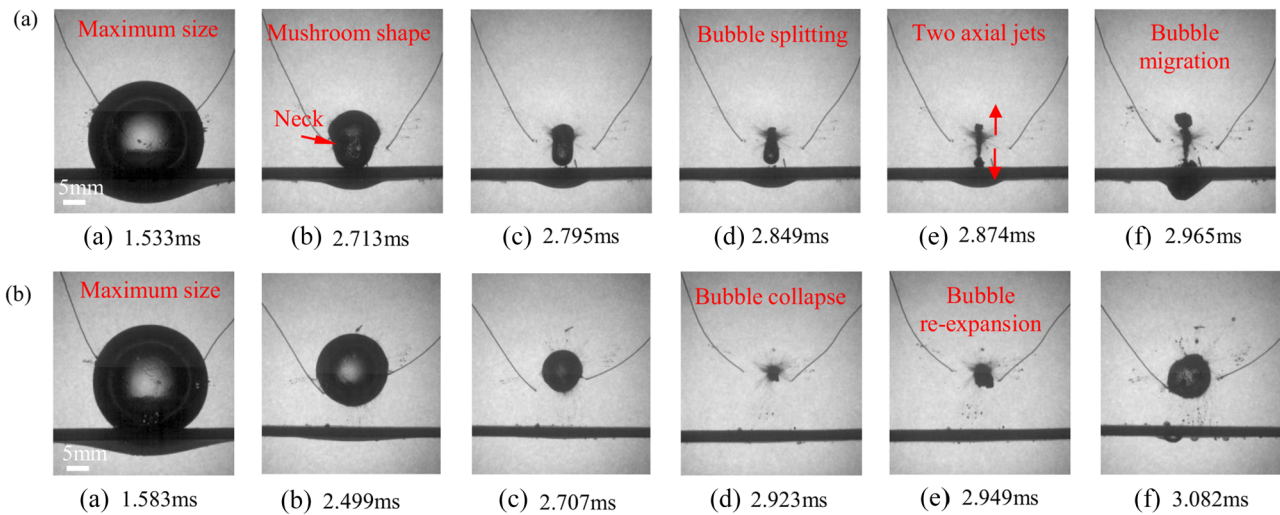


FIG. 4. Behaviors of cavitation bubbles after reaching their maximum sizes at $d' = 0.00911$ (sample 3): (a) formation of two axial jets at $h^* = 0.5$ and (b) no jets at $h^* = 1.0$. In (a) and (b), frame (1) represents the time when the bubble reaches its maximum size. Multimedia view: <https://doi.org/10.1063/5.0107339.2>; (b) <https://doi.org/10.1063/5.0107339.3>

classified into two groups: (i) the formation of two axial jets and (ii) no jets, as shown in Fig. 4. In the works of Brujan *et al.*,^{25,26} a jet directing away from the membrane was induced at a large h^* , which was not observed in this study. This was due to the softer and thinner boundary used in the experiments. At $h^* = 0.5$, the bubble developed a mushroom-like shape, elongated, and split into two small bubbles (upper bubble and lower bubble) from the position of the neck. The small bubbles clearly migrated upward and downward due to the two induced axial jets. The downward jet impacted the membrane and induced its large deformation, as seen in frame (6) of Fig. 4(a) (multimedia view). At $h^* = 1.0$, it was found that the bubble oscillated spherically during the first and second pulsation, although a slight deformation of the membrane was induced at the expansion stage, and bubble migration hardly occurred, as seen in Fig. 4(b) (multimedia view).

Subsequently, we analyzed the migration of the upper bubble induced by the upward jet by extracting the bubble's highest-point vertical displacement since the bubble splitting, as shown in Fig. 3 and Fig. 5. The value of h^* ranged from 0.4 to 1.0. The abscissa is the time ($t - t_{collapse}$) and $t_{collapse}$ was 2.486, 2.594, 2.507, 2.546, 2.484, and 2.627 ms at $h^* = 0.4, 0.5, 0.6, 0.7, 0.8,$ and 1.0 , respectively. The ordinate is the vertical displacement of the highest point, and the zero-point is the neck position when the bubble splits in the respective case. At $h^* = 0.8$ and 1.0 , two axial jets were not induced, whereas they formed at $h^* = 0.4, 0.5, 0.6,$ and 0.7 . At $h^* = 0.8$ and 1.0 , the vertical displacements of the highest points first increased immediately after bubble splitting due to the re-expansion of the bubble, then reached a maximum, and finally maintained their positions when the bubble reached the maximum size during the second pulsation. In the cases of jet formation, it was found that the maximum vertical displacement decreased as h^* increased, which indicated that the energy of the upward migration decreased. Compared with the cases of no jets, the maximum vertical displacements were much larger under the action of the axial

jets. Consequently, the axial jets resulted in obvious migration of the cavitation bubble.

We investigated the neck position when the bubble split for various h^* values, as shown in Fig. 6. As h^* increased, the dimensionless neck position L' decreased, and the position of the neck moved far away from the soft membrane, which indicated that the energy and volume of the upper bubble decreased, and thus, the upward migration decreased.

As mentioned above, the counteracting force induced by the rebounding of the membrane (F) was a dominant factor in developing a mushroom-shaped bubble and two axial jets. The

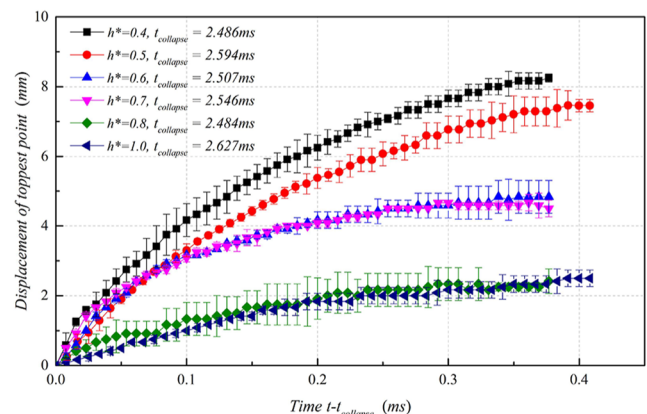


FIG. 5. Time variations with highest-point vertical displacements of cavitation bubbles after bubble splitting at $d' = 0.00911$ (sample 3) for various h^* values. Experimental data are analyzed from $h^* = 0.4$ because the neck is not observed at a smaller h^* due to the blocking of the membrane when the bubble splits. At $h^* = 0.8$ and 1.0 , the jets were not induced, whereas they formed at $h^* = 0.4, 0.5, 0.6,$ and 0.7 . Measurement uncertainty is described in Sec. II.

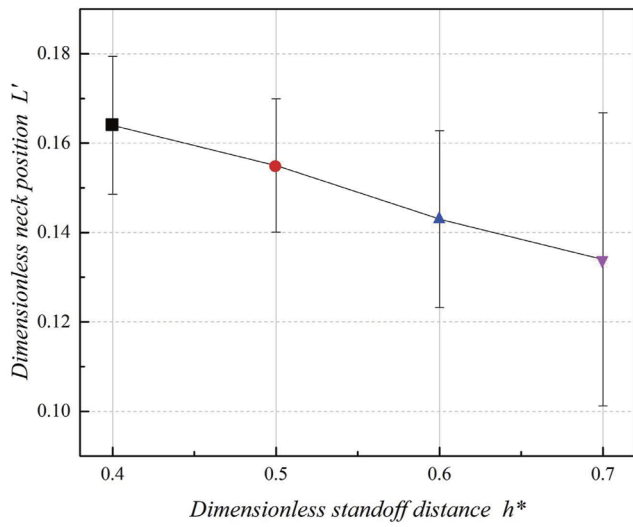


FIG. 6. Relationship between L' and h^* at $d' = 0.009\ 11$ (sample 3). The dimensionless neck position L' is $L' = L_p/L$, where L_p is the distance between the bubble point and the neck position, and L is the bubble length at the moment of bubble collapse. Measurement uncertainty is described in Sec. II.

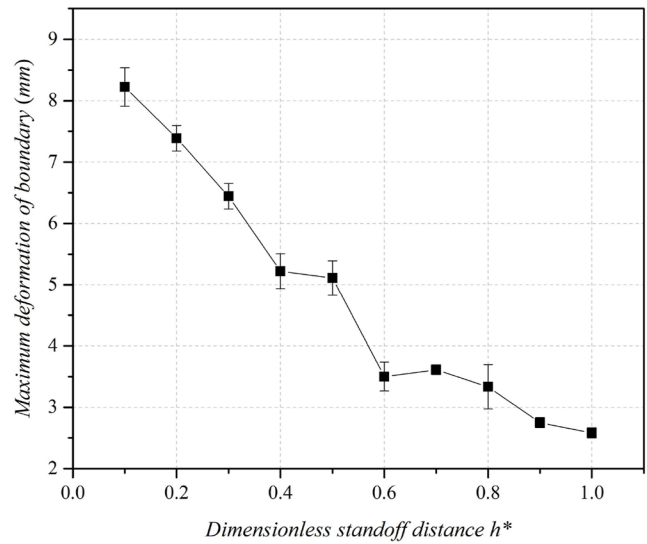


FIG. 7. Maximum membrane deformation during bubble expansion for various h^* values. The zero-point of the ordinate is the lower surface of the membrane. Measurement uncertainty is described in Sec. II.

counteracting force is described by $F \sim wd^3$, where w and d are the deflection and thickness of the membrane, respectively. w is described using the maximum deformation of the membrane. Figure 7 shows the maximum membrane deformation during bubble expansion for various h^* values. As h^* increased, the maximum deformation decreased. As a result, the counteracting force decreased because the membrane thickness d was constant so that

the volume of the upper bubble and the upward migration both decreased.

C. Effects of dimensionless stiffness d' on the formation of two axial jets

The dimensionless stiffness (d') was varied by changing the thickness of the Ecoflex membrane. The experimental results

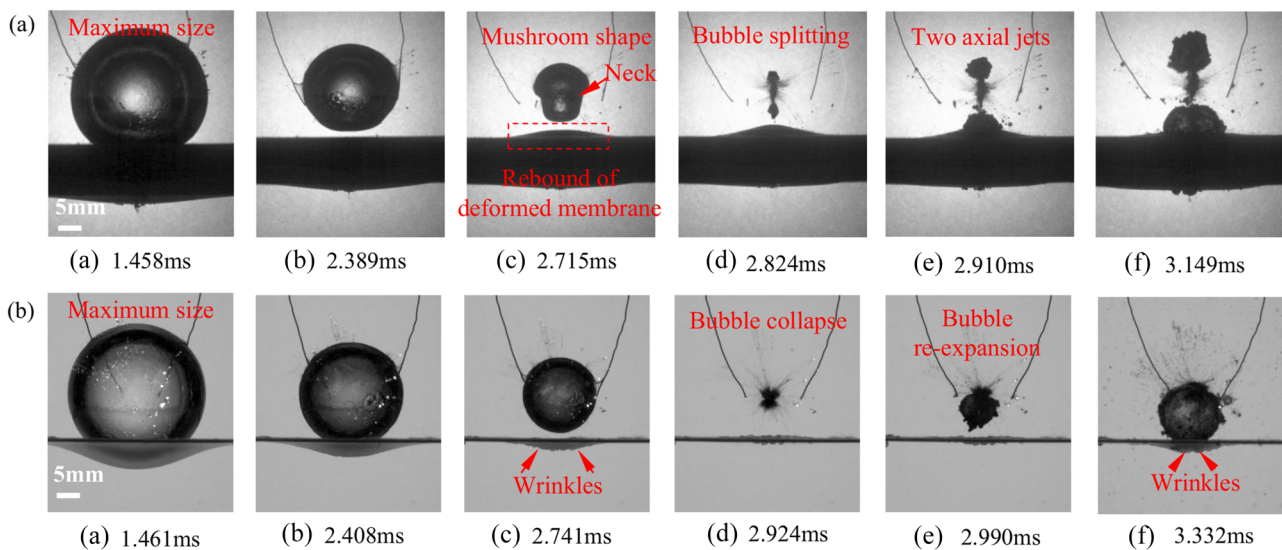


FIG. 8. Behaviors of cavitation bubbles after reaching their maximum sizes at $h^* = 0.7$ for various d' values: (a) formation of two axial jets at $d' = 0.018\ 22$ (sample 11) and (b) no jets at $d' = 0.001\ 37$ (sample 1). In (a) and (b), frame (1) represents the time when the bubble reached its maximum size. Multimedia view: <https://doi.org/10.1063/5.0107339.4>; (b) <https://doi.org/10.1063/5.0107339.5>

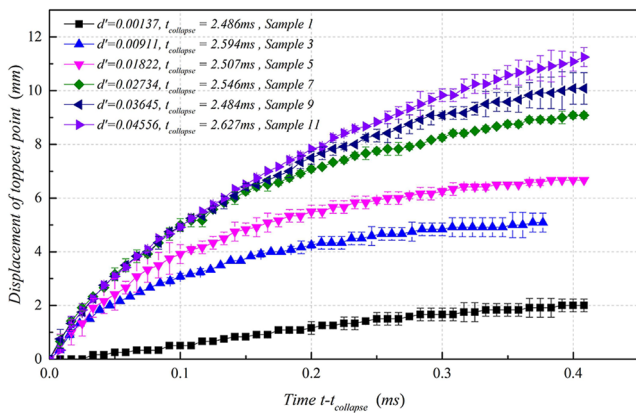


FIG. 9. Time variations with highest point vertical displacements of cavitation bubbles after bubble splitting at $h^* = 0.7$ for various d' . At $d' = 0.00137$ and 0.00456 , two axial jets were not induced, while they formed at $d' = 0.00911, 0.02734, 0.04556, 0.01822,$ and 0.03645 . Measurement uncertainty is described in Sec. II.

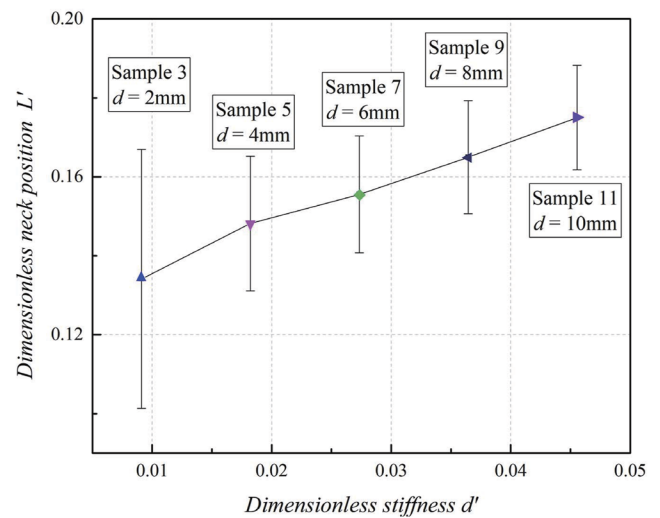


FIG. 10. Relationship between L' and h^* at $h^* = 0.7$. Measurement uncertainty is described in Sec. II.

showed that the bubble dynamics were characterized by the formation of two axial jets and no jets for various d' values. As shown in Fig. 8(a) (multimedia view), the expansion of the cavitation bubble resulted in the downward deformation of the membrane. As the bubble contracted, the deformed membrane rebounded, and upward deformation is observed in frame (3). Meanwhile, a mushroom-like-shaped bubble developed. Two axial jets were induced when the bubble split, with one directing toward and the other away from the membrane. At $d' = 0.00137$, the bubble collapsed approximately spherically during the entire process. Wrinkles at the membrane surface occurred during the process of bubble contraction and re-expansion, which were induced by interfacial instability and were a unique phenomenon only occurring near a 3 mm-thick

membrane, as shown in Fig. 8(b) (multimedia view). Briefly, a large thickness of a soft membrane improves the generation of two axial jets.

As mentioned in Fig. 5, the upward migration was described using the vertical displacement of the highest point of the upper bubble after the bubble split. The time variation with vertical displacement for various d' values is shown in Fig. 9. The abscissa is the time $t-t_{collapse}$, and $t_{collapse}$ was 2.928, 2.837, 2.733, 2.538, 2.707, 2.624, and 2.770 ms at $d' = 0.00911, 0.02734, 0.04556, 0.01822, 0.03645, 0.00137,$ and 0.00456 , respectively. The ordinate is the vertical displacement of the highest point, and the zero-point is

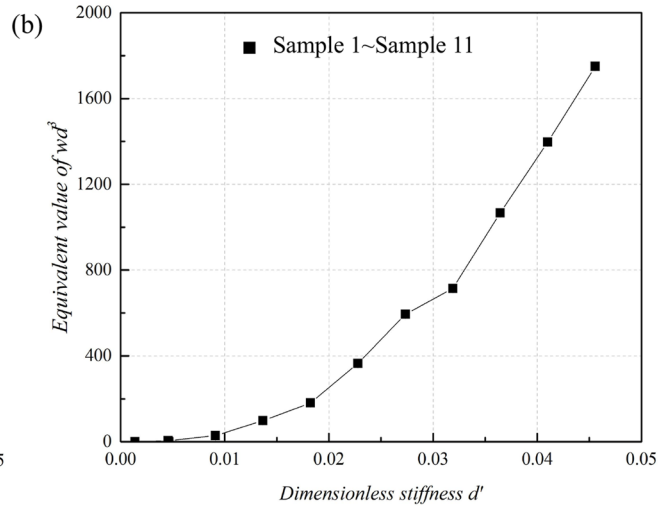
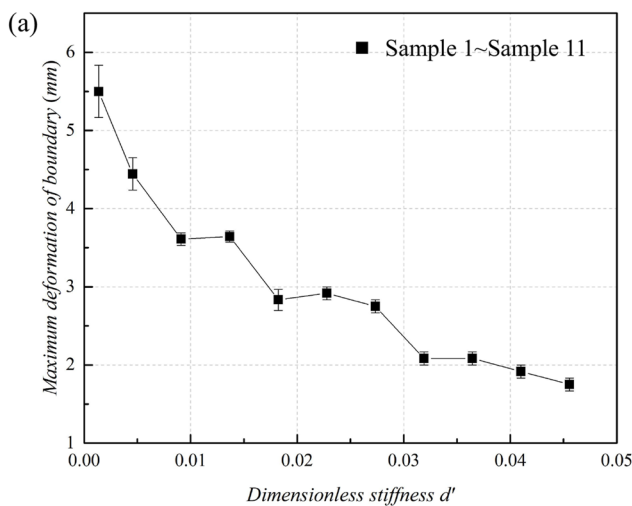


FIG. 11. Maximum membrane deformation during bubble expansion (a) and equivalent values of wd^3 (b) for various h^* values. In (a), the zero-point of the ordinate is the lower surface of the membrane. Measurement uncertainty is described in Sec. II.

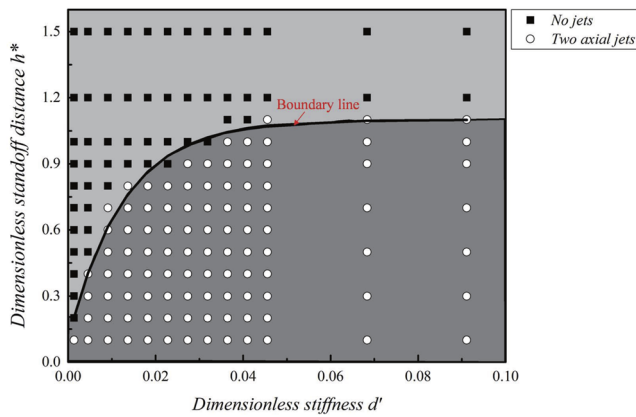


FIG. 12. Phase diagram of bubble jetting near a soft membrane: (i) formation of two axial jets and (ii) no jets. The abscissa and ordinate are the dimensionless stiffness d' and stand-off distance h^* , respectively. The black line denotes the boundary line between the regimes of no jets and two axial jets.

the neck position when the bubble splits in the respective case. At $d' = 0.00137$ and 0.00456 , the vertical displacements of the highest points first increased immediately after bubble splitting due to the re-expansion of the bubble, then reached a maximum, and finally

maintained the positions when the bubble reached its maximum size during the second pulsation. In the cases of jet formation, with an increase in d' , the upward migration increased, which indicated the volume and energy of the upper bubble increased as d' increased. Consequently, we investigated the relationship of L' and d' , as shown in Fig. 10. With an increase in d' , L' increased, and the position of the neck when the bubble split moved closer to the membrane. As a result, the upward migration strengthened with increasing d' .

We measured the magnitude of the counteracting force for various d' values. Figure 11(a) shows the maximum membrane deformation during the bubble expansion. It was found that the deformation maximum was inversely proportional to the value of d' . However, a large d' indicated a thick membrane. According to formula $F \sim wd^3$, the force strengthened with increasing d' , as shown in Fig. 11(b). As a result, a thick membrane increased the magnitude of the counteracting force, thus strengthening the bubble splitting and formation of two axial jets.

D. On the criteria of axial jet formation and boundary piercing

The experimental observations of the bubble dynamics near the soft membranes were obtained at various values of h^* and d' . A phase diagram is obtained depending on the formation of the

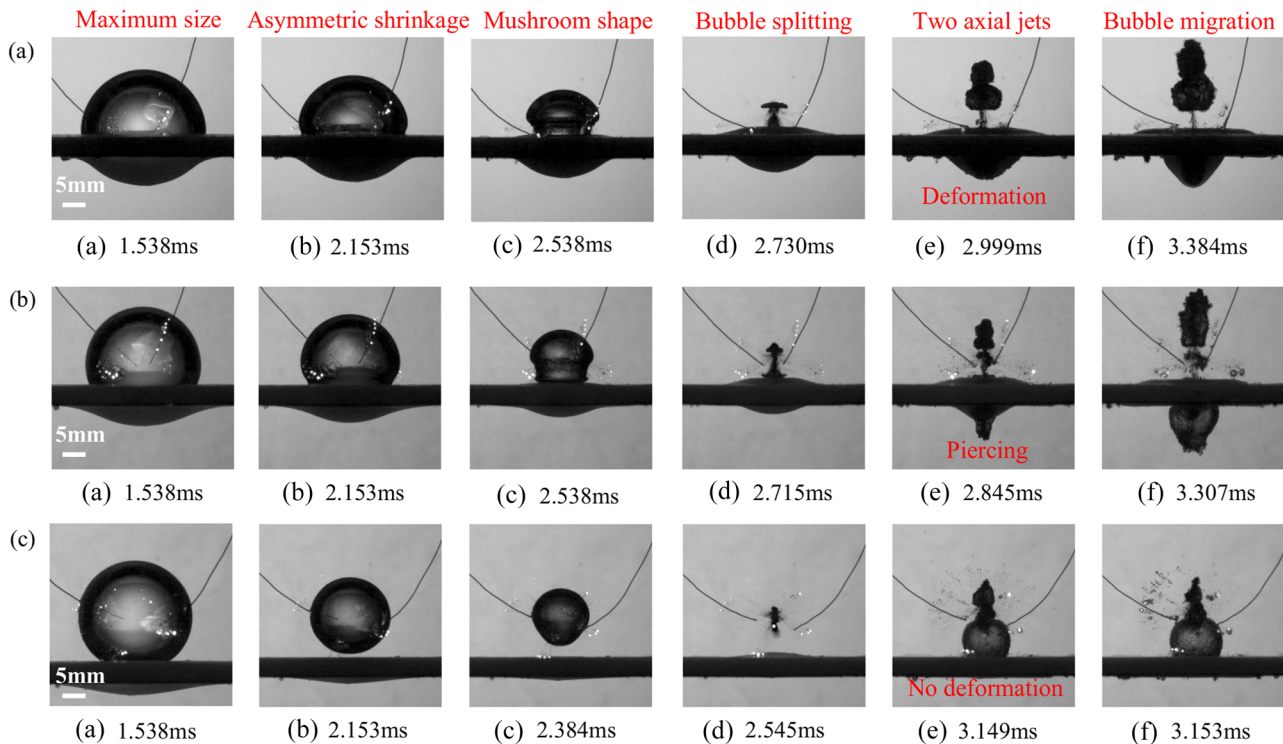


FIG. 13. Behaviors of the membranes induced by the impact of the downward jet at $d' = 0.01822$ (sample 5): (a) large deformation of the membrane at $h^* = 0.1$, (b) piercing of the membrane at $h^* = 0.4$, and (c) no deformation at $h^* = 0.8$. The first frames in (a), (b), and (c) describe the time when the cavitation bubble reached its maximum size. Multimedia view: <https://doi.org/10.1063/5.0107339.6>; (b) <https://doi.org/10.1063/5.0107339.7>; (c) <https://doi.org/10.1063/5.0107339.8>

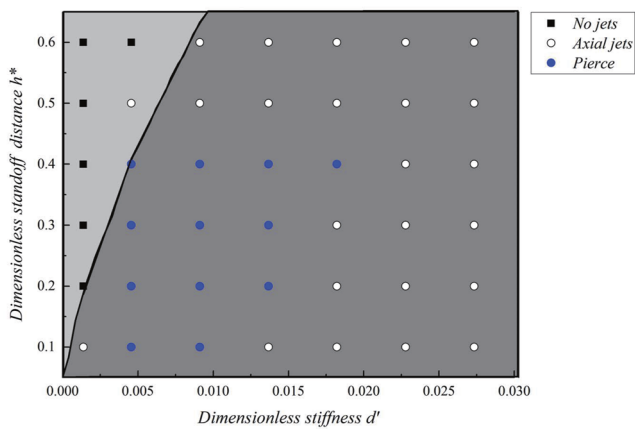


FIG. 14. Sub-regime of membrane piercing in the regime of two axial jets. The red line denotes the boundary line between the regimes of no jets and two axial jets. The blue circles represent membrane piercing. The white circles represent the formation of two axial jets but no membrane piercing. The black squares represent no jets.

two axial jets, as shown in Fig. 12, where the abscissa and ordinate are the dimensionless stiffness d' and stand-off distance h^* , respectively. The symbols of black solid squares and white solid circles represent the phenomena of no jet and two axial jets, respectively. When h^* was larger than a critical value, the axial jets were not induced; this is denoted as the critical h^* . In the case of $d' = 0.00137$, the axial jets were induced at an h^* value smaller than 0.1. The thin membrane (0.3 mm thickness) used in this case resulted in a weak counteracting force during the bubble collapse. As mentioned above, the counteracting force strengthened

with increasing d' . Consequently, critical h^* increased exponentially, reaching a maximum of 1.1 at $d' = 0.04556$. After that, critical h^* remained constant because the membrane deformation changed from global deformation to local deformation. Furthermore, the magnitude of the local deformation was much less than the membrane thickness and was constant as d' increased, which suggested that the counteracting force was independent of the membrane thickness and directly proportional to the membrane deformation. As a result, the boundary line between the regimes of no jets and two axial jets was an exponential function, as shown in the following equation:

$$h^* = -e^{C_1 d'} + 1.1, \tag{5}$$

where the value of 1.1 indicates the maximum value of the critical h^* for the Ecoflex membrane, and C_1 is a constant related to the material properties of the soft membrane. We determine that $C_1 = -79.4$ by fitting the experimental results.

After the bubble splitting, the downward jet impacted the membrane and resulted in the deformation and even piercing of the membrane. Figure 13 shows the behaviors of the membranes after the jet impact at $h^* = 0.1, 0.4$, and 0.8 . At $h^* = 0.1$, a large deformation was induced by the impact of the axial jet, but membrane piercing did not occur, as shown in Fig. 13(a) (multimedia view). At $h^* = 0.4$, the membrane was pierced after the impact. The lower bubble passed through the pierced hole and re-expanded under the membrane, as shown in Fig. 13(b) (multimedia view). At $h^* = 0.8$, the jet impact could not induce an obvious deformation of the membrane, as shown in Fig. 13(c) (multimedia view). Therefore, we obtained a sub-regime of the membrane piercing in the regime of two axial jets, as shown in Fig. 14. Membrane piercing occurred when d' ranged from 0.00456 to 0.01822. Overall, membrane piercing was induced at h^* values smaller than 0.4. We also observed that the downward jet could not pierce the

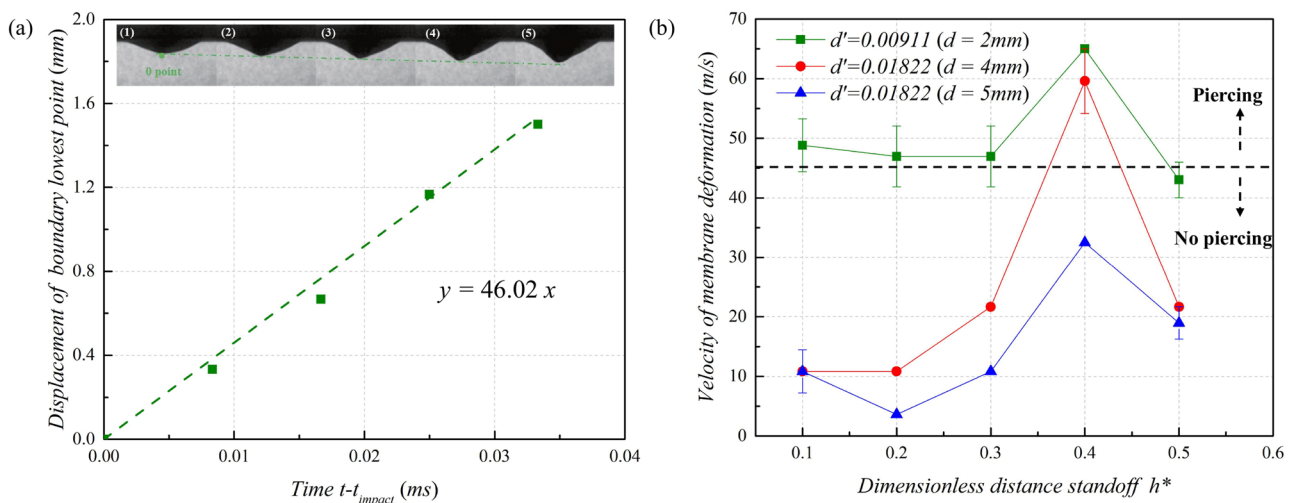


FIG. 15. Velocities of membrane deformation from the impact of the downward jet: (a) time variation with the displacements of the membrane's lowest points and (b) the critical condition inducing membrane piercing. In (a), the abscissa and ordinate are the displacement of the membrane's lowest point and the time, respectively. In (b), the abscissa and ordinate are the dimensionless distance and velocity of membrane deformation, respectively. Measurement uncertainty is described in Sec. II.

membrane at an h^* value smaller than 0.4 at $d' = 0.01367$ and 0.01822. As described by Deris and Nadler,⁴⁶ a soft membrane is pierced when the resultant strain energy exceeds the peak value. The resultant strain energy is related to the velocity of the membrane deformation.

We investigated the displacements of the lowest point at the lower surface of the membrane within the time interval from the impact of the axial jet to the piercing of the membrane, as shown in Fig. 15(a). The displacement was directly proportional to the time. The velocities of the membrane deformation induced by the impact of the jet are obtained by linear fitting.

The velocity of the membrane deformation was determined by the impact velocity of the downward jet when $d' = \text{const}$. The impact velocity depended on the energy of the lower bubble and the distance between the neck position and the membrane when the bubble split. As shown in Fig. 6, L' decreased as h^* increased, which suggested that the volume and energy of the lower bubble increased, so that the downward jet velocity increased. However, a large distance between the neck position and the membrane weakens the impact velocity of the jet. As a result, the membrane deformation velocity increased first with increasing h^* and reached a maximum at $h^* = 0.4$, and then decreased, as shown in Fig. 15(b). This was the reason why membrane piercing was induced at h^* values smaller than 0.4, and why there were cases where the downward jet could not pierce the membrane at a smaller h^* , as shown in Fig. 14.

On the other hand, according to the relationship between L' and d' , the volume and energy of the lower bubble decreased, so the downward jet velocity decreased as d' increased. Moreover, a large thickness prevented membrane deformation from the jet impact. Consequently, the velocity of membrane deformation decreased as d' increased when $h^* = \text{const}$, which was why the downward jet could not pierce the boundary at d' values larger than 0.01822 ($d = 4$ mm). Given the results in Fig. 15(b), we determine that the critical velocity of membrane deformation inducing the piercing of the membrane was ~ 45 m/s.

IV. CONCLUSIONS

We experimentally investigated the formation of two axial jets of a cavitation bubble near an Ecoflex membrane with different thicknesses. In the experiments, a cavitation bubble was generated using an underwater electric discharge machine. The dominant dimensionless parameters determining the formation of the two axial jets were obtained, the stiffness (d') and stand-off distance (h^*), assuming that the millimeter-sized bubble was filled with an ideal gas and collapsed adiabatically in water.

After the bubble split, two axial jets flowing in opposite directions formed, resulting in obvious upward and downward migration. We obtain two parameter plots for the regimes of two axial jets and no jets. The critical h^* of the jet formation increased exponentially with increasing d' , reaching a maximum of 1.1 at $d' = 0.04556$ ($d = 10$ mm). This was because the counteracting force induced by the rebounding of the deformed membrane was strengthened. After that, the critical h^* remained constant because the counteracting force was unchanged due to the pattern change of the membrane deformation. As a result, we obtain a function of the boundary line between the regimes.

In the regime of two axial jets, a dimension neck position L' is defined to determine the energy distribution of upward and downward migrations. Experimental observations showed that a larger L' suggested that the neck position moved closer to the membrane and thus caused larger upward migration. After the impact of the jet, the membrane deformed and was even pierced. A sub-regime of membrane piercing is obtained in the regime. It was found that the velocity of membrane deformation was an important factor in determining membrane piercing. According to the relationship between h^* and L' , the jet velocity increased with increasing h^* . However, a longer distance between the neck position and membrane weakened the jet velocity. Therefore, the velocity of membrane deformation increased, reached a maximum at $h^* = 0.4$, and then decreased when $d' = \text{const}$. As d' increased, L' increased, and thus, the jet velocity decreased. Moreover, a large d' prevented membrane deformation. The velocity of the membrane deformation decreased with increasing d' when $L' = \text{const}$. Finally, a critical velocity of membrane deformation inducing membrane piercing of ~ 45 m/s was obtained.

This study determined the conditions of jet formation and membrane piercing from a cavitation bubble near a soft membrane, and it provides a reference in some fields, such as intraocular photodisruption and laser myocardial revascularization. In this study, the dimensionless stiffness d' was varied by changing the membrane thickness. Therefore, it is of great interest to investigate bubble jetting and membrane piercing in terms of the properties of the membrane.

ACKNOWLEDGMENTS

This work was supported by the National Natural Science Foundation of China (Grant Nos. 12122214 and 11902323), the Young Elite Scientists Sponsorship Program by CAST (Grant No. 2019QNRC001), and the Youth Innovation Promotion Association CAS (Grant Nos. 2022019 and Y201906).

AUTHOR DECLARATIONS

Conflict of Interest

The authors have no conflicts to disclose.

Author Contributions

Ao Wang: Conceptualization (equal); Data curation (equal); Formal analysis (equal); Investigation (equal); Methodology (equal); Project administration (equal). **Yuxue Zhong:** Conceptualization (equal); Data curation (equal); Formal analysis (equal). **Guang-hang Wang:** Conceptualization (equal); Data curation (equal); Formal analysis (equal); Investigation (supporting). **Jian Huang:** Conceptualization (equal); Data curation (equal); Formal analysis (equal). **Jingzhu Wang:** Investigation (equal). **Yiwei Wang:** Conceptualization (equal); Data curation (equal); Formal analysis (equal).

DATA AVAILABILITY

The data that support the findings of this study are available from the corresponding author upon reasonable request.

REFERENCES

- ¹Q. Zeng, H. An, and C. D. Ohl, "Wall shear stress from jetting cavitation bubbles: Influence of the stand-off distance and liquid viscosity," *J. Fluid Mech.* **932**, A14 (2022).
- ²Q. Zeng, S. R. Gonzalez-Avila, R. Dijkink, P. Koukouvinis, M. Gavaises, and C.-D. Ohl, "Wall shear stress from jetting cavitation bubbles," *J. Fluid Mech.* **846**, 341 (2018).
- ³S. Li, A. M. Zhang, R. Han, and Y. Q. Liu, "Experimental and numerical study on bubble-sphere interaction near a rigid wall," *Phys. Fluids* **29**, 092102 (2017).
- ⁴S.-P. Wang, A.-M. Zhang, Y.-L. Liu, S. Zhang, and P. Cui, "Bubble dynamics and its applications," *J. Hydrodyn.* **30**, 975 (2018).
- ⁵Y. Sun, Y. Du, Z. Yao, Q. Zhong, S. Geng, and F. Wang, "The effect of surface geometry of solid wall on the collapse of a cavitation bubble," *J. Fluids Eng.* **144**, 071402 (2022).
- ⁶P. Xu, S. Liu, Z. Zuo, and Z. Pan, "On the criteria of large cavitation bubbles in a tube during a transient process," *J. Fluid Mech.* **913**, R6 (2022).
- ⁷S. Li, A.-M. Zhang, and R. Han, "Counter-jet formation of an expanding bubble near a curved elastic boundary," *Phys. Fluids* **30**, 121703 (2018).
- ⁸A. Vogel, "Nonlinear absorption: Intraocular microsurgery and laser lithotripsy," *Phys. Med. Biol.* **42**, 895 (1997).
- ⁹T. Požar and R. Petkovšek, "Cavitation induced by shock wave focusing in eye-like experimental configurations," *Biomed. Opt. Express* **11**, 432 (2020).
- ¹⁰*TMLR Management of Coronary Artery Diseases*, edited by M. Klein, H. D. Schulte, and E. Gams (Springer Science & Business Media, 2012).
- ¹¹R. Brinkmann, D. Theisen, T. Brendel, and R. Birngruber, "Single-pulse 30-J holmium laser for myocardial revascularization—a study on ablation dynamics in comparison to CO₂ laser-TMR," *IEEE J. Sel. Top. Quantum Electron.* **5**, 969 (1999).
- ¹²E. Klaseboer and B. C. Khoo, "An oscillating bubble near an elastic material," *J. Appl. Phys.* **96**, 5808 (2004).
- ¹³B. Dollet, P. Marmottant, and V. Garbin, "Bubble Dynamics in soft and biological matter," *Annu. Rev. Fluid Mech.* **51**, 331 (2019).
- ¹⁴M. T. Shervani-Tabar, A. Hajizadeh Aghdam, B. C. Khoo, V. Farhangmehr, and B. Farzaneh, "Numerical analysis of a cavitation bubble in the vicinity of an elastic membrane," *Fluid Dyn. Res.* **45**, 055503 (2013).
- ¹⁵X. Ma, B. Huang, X. Zhao, Y. Wang, Q. Chang, S. Qiu, X. Fu, and G. Wang, "Comparisons of spark-charge bubble dynamics near the elastic and rigid boundaries," *Ultrason. Sonochem.* **43**, 80 (2018).
- ¹⁶Q. Yu, Z. Xu, J. Zhao, M. Zhang, and X. Ma, "PIV-based acoustic pressure measurements of a single bubble near the elastic boundary," *Micromachines* **11**, 637 (2020).
- ¹⁷D. Horvat, U. Orthaber, J. Schille, L. Hartwig, U. Löschner, A. Vrečko, and R. Petkovšek, "Laser-induced bubble dynamics inside and near a gap between a rigid boundary and an elastic membrane," *Int. J. Multiphase Flow* **100**, 119 (2018).
- ¹⁸M. Koch, J. M. Rosselló, C. Lechner, W. Lauterborn, and R. Mettin, "Dynamics of a laser-induced bubble above the flat top of a solid cylinder—Mushroom-shaped bubbles and the fast jet," *Fluids* **7**, 2 (2021).
- ¹⁹S. Li, A.-M. Zhang, R. Han, and Q. Ma, "3D full coupling model for strong interaction between a pulsating bubble and a movable sphere," *J. Comput. Phys.* **392**, 713 (2019).
- ²⁰D. C. Gibson, "Cavitation adjacent to plane boundaries," in Proceedings 3rd Australasian Conference on Hydraulics and Fluid Mechanics, 1968.
- ²¹D. C. Gibson and J. R. Blake, "Growth and collapse of cavitation bubbles near flexible boundaries," in Proceedings 7th Australasian Conference on Hydraulics and Fluid Mechanics, 1980.
- ²²D. C. Gibson and J. R. Blake, "The growth and collapse of bubbles near deformable surfaces," *Appl. Sci. Res.* **38**, 215 (1982).
- ²³J. R. Blake and D. C. Gibson, "Cavitation bubbles near boundaries," *Annu. Rev. Fluid Mech.* **19**, 99 (1987).
- ²⁴Y. Tomita and T. Kodama, "Interaction of laser-induced cavitation bubbles with composite surfaces," *J. Appl. Phys.* **94**, 2809 (2003).
- ²⁵A. Shima, Y. Tomita, D. C. Gibson, and J. R. Blake, "The growth and collapse of cavitation bubbles near composite surfaces," *J. Fluid Mech.* **203**, 199 (1989).
- ²⁶E.-A. Brujan, K. Nahen, P. Schmidt, and A. Vogel, "Dynamics of laser-induced cavitation bubbles near an elastic boundary," *J. Fluid Mech.* **433**, 251 (2001).
- ²⁷E.-A. Brujan, K. Nahen, P. Schmidt, and A. Vogel, "Dynamics of laser-induced cavitation bubbles near elastic boundaries: Influence of the elastic modulus," *J. Fluid Mech.* **433**, 283 (2001).
- ²⁸E. A. Brujan, K. Nahen, P. Schmidt, and A. Vogel, "Dynamics of laser-induced cavitation bubbles near an elastic boundary used as a tissue phantom," *AIP Conf. Proc.* **524**, 381 (2000).
- ²⁹S. J. Shaw, Y. H. Jin, T. P. Gentry, and D. C. Emmony, "Experimental observations of the interaction of a laser generated cavitation bubble with a flexible membrane," *Phys. Fluids* **11**, 2437 (1999).
- ³⁰C. K. Turangan, G. P. Ong, E. Klaseboer, and B. C. Khoo, "Experimental and numerical study of transient bubble-elastic membrane interaction," *J. Appl. Phys.* **100**, 054910 (2006).
- ³¹U. Orthaber, R. Petkovšek, J. Schille, L. Hartwig, G. Hawlina, B. Drnovšek-Olup, A. Vrečko, and I. Poberaj, "Effect of laser-induced cavitation bubble on a thin elastic membrane," *Opt. Laser Technol.* **64**, 94 (2014).
- ³²W. Xu, Y. Zhai, J. Luo, Q. Zhang, and J. Li, "Experimental study of the influence of flexible boundaries with different elastic moduli on cavitation bubbles," *Exp. Therm. Fluid Sci.* **109**, 109897 (2019).
- ³³A. Hajizadeh Aghdam, S. W. Ohl, B. C. Khoo, M. T. Shervani-Tabar, and M. R. H. Nobari, "Effect of the viscosity on the behavior of a single bubble near a membrane," *Int. J. Multiphase Flow* **47**, 17 (2012).
- ³⁴Ž. Lokar, R. Petkovšek, and M. Dular, "Cavitation bubble dynamics in a vicinity of a thin membrane wetted by different fluids," *Sci. Rep.* **11**, 3506 (2021).
- ³⁵X.-Y. Kan, J.-L. Yan, S. Li, and A.-M. Zhang, "Rupture of a rubber sheet by a cavitation bubble: An experimental study," *Acta Mech. Sin.* **37**, 1489 (2021).
- ³⁶R. Han, A. M. Zhang, S. Tan, and S. Li, "Interaction of cavitation bubbles with the interface of two immiscible fluids on multiple time scales," *J. Fluid Mech.* **932**, A8 (2022).
- ³⁷P. Cui, A. M. Zhang, S. P. Wang, and Y. L. Liu, "Experimental study on interaction, shock wave emission and ice breaking of two collapsing bubbles," *J. Fluid Mech.* **897**, A25 (2020).
- ³⁸A. S. Nechyporenko, S. S. Krivenko, V. Alekseeva, A. Lupyr, N. Yurevych, R. S. Nazaryan, and V. V. Gargin, "Uncertainty of measurement results for anatomical structures of paranasal sinuses," in *IEEE 8th Mediterranean Conference on Embedded Computing (MECO)* (IEEE, 2019).
- ³⁹Y. Shi, Y. Hua, and G. Pan, "Experimental study on the trajectory of projectile water entry with asymmetric nose shape," *Phys. Fluids* **32**, 122119 (2020).
- ⁴⁰S. D. Guleria, A. Dhar, and D. V. Patil, "Experimental insights on the water entry of hydrophobic sphere," *Phys. Fluids* **33**, 102109 (2021).
- ⁴¹C. Lugni, J. Wang, O. M. Faltinsen, A. Bardazzi, A. Lucarelli, and W. Duan, "Scaling laws for the water entry of a three-dimensional body," *Phys. Fluids* **33**, 036104 (2021).
- ⁴²Q. Zeng, S. R. Gonzalez-Avila, and C. D. Ohl, "Splitting and jetting of cavitation bubbles in thin gaps," *J. Fluid Mech.* **896**, A28 (2020).
- ⁴³C. Lechner, W. Lauterborn, M. Koch, and R. Mettin, "Fast, thin jets from bubbles expanding and collapsing in extreme vicinity to a solid boundary: A numerical study," *Phys. Fluids* **4**, 021601 (2019).
- ⁴⁴C. Lechner, W. Lauterborn, M. Koch, and R. Mettin, "Jet formation from bubbles near a solid boundary in a compressible liquid: Numerical study of distance dependence," *Phys. Rev. Fluids* **5**, 093604 (2020).
- ⁴⁵S. Weinbaum, L. Chen, and P. Ganatos, "Elastohydrodynamic collision and rebound of a flat plate from a planar surface due to body and fluid inertia," *Phys. Fluids* **1**, 140 (1989).
- ⁴⁶A. H. A. Deris and B. Nadler, "Modeling the indentation and puncturing of inflated elastic membranes by rigid indenters," *Int. J. Nonlinear Mech.* **69**, 29 (2015).